Scripta Materialia 172 (2019) 66–71

Contents lists available at ScienceDirect

Scripta Materialia

journal homepage: www.elsevier.com/locate/scriptamat

High impact toughness of CrCoNi medium-entropy alloy at liquid-helium temperature

Muxin Yang [a], Lingling Zhou [a], Chang Wang [b], Ping Jiang [a], Fuping Yuan [a,d], Evan Ma [c,*], Xiaolei Wu [a,d,**]

[a] State Key Laboratory of Nonlinear Mechanics, Institute of Mechanics, Chinese Academy of Sciences, Beijing 100190, China
[b] Central Laboratory, Central Iron and Steel Research Institute, Beijing 100081, China
[c] Department of Materials Science and Engineering, Johns Hopkins University, Baltimore, MD 21218, USA
[d] School of Engineering Science, University of Chinese Academy of Sciences, Beijing 100049, China

ARTICLE INFO

Article history:
Received 25 March 2019
Received in revised form 8 July 2019
Accepted 9 July 2019
Available online xxxx

Keywords:
Impact fracture toughness
Twinning
Ductility
High-entropy alloy
Strain hardening

ABSTRACT

We show that face-centered-cubic CrCoNi medium-entropy alloy sustains a Charpy V-notch impact toughness (A_K) as high as 340 J at 4 K. Deformation twinning (DT) is rendered exceptionally profuse by this alloy's low stacking fault energy, combined with liquid-helium temperature and high strain rates that both incur high stresses to favor DT across a large plastic zone. This efficiently dissipates imposed mechanical energy, accumulates defects to sustain high strain hardening, and restrains strain localization events from evolving into major shear bands. Martensitic transformation to hexagonal phase is insignificant. CrCoNi is therefore a strong competitor to the best existing cryogenic alloys.

Materials in extreme environments are currently attracting much attention. In this regard, the combination of impact loading (high strain rates) and ultra-low temperatures is highly demanding on fracture toughness, i.e., the ability of a material to resist cracking under stresses [1–3]. Cryogenic environments below liquid nitrogen temperature (LNT, 77 K) are encountered during the exploration of outer space (e.g., Pluto can reach a temperature as low as 40 K), or the operation of many types of superconductors with a critical temperature below LNT. Temperatures near the liquid helium temperature (LHT, 4.2 K) and impact loading rates pose additional challenges to materials selection, as the repertoire of the suitable alloys is currently very limited. Previously reported Charpy impact fracture toughness (A_K) data, assessed using the ASTM E23 full-sized (i.e., $10 \times 10 \times 55$ mm^3) sample for cryogenic alloys at LNT and LHT, are summarized in Fig. 1a (see also Supplementary Fig. S1 for details). Only a couple of these alloys can preserve respectable A_K on the order of 100 J when temperature decreases towards 4.2 K [4,5]. This is considerably lower than the A_K values of these same alloys at room temperature (RT), the best of which can approach 300 J [6–8].

Intrinsic toughening relies on plastic deformation and work hardening in the plastic zone ahead of the crack tip, to dissipate energy to retard crack propagation [2,3]. However, these processes become difficult to operate at low temperatures especially in the body-centered-cubic alloys, causing the ductile-to-brittle transition (DBT) [9,10]. The DBT is less of a problem in face-centered-cubic (fcc) metals (such as austenitic stainless steels commonly used as cryogenic alloys), which have ample slip systems that are easily activated [4,5]. Dislocations and deformation twinning (DT) remain operative at cryogenic temperatures, and the storage of these defects and the difficulty of cross-slip lead to pronounced strain hardening. Nonetheless, A_K at LHT is generally not as high as that at RT. 304-type stainless steels, for instance, undergo strain-induced martensitic transformation, especially at low temperatures, producing the body-centered tetragonal α' and hexagonal ε phases that constitute a considerable fraction of the microstructure [4,5]. While moderate phase transformation may increase the toughness, the extent of impact-induced martensite can become too great ahead of the crack tip to degrade A_k [4,5].

Recently developed single-phase high- and medium-entropy alloys (HEA/MEA) [11–24] may be suitable for use in the LNT-LHT range. They have already been demonstrated to show high fracture toughness (K_{IC}) [14,18,19] from RT to 77 K, attributed to their low stacking fault energy (SFE) [19], and high propensity of DT [13,18–21]. The high density of nanoscale twins formed during deformation causes dramatic strain hardening [13,18–21,23,25–27] in the plastic zone ahead of the crack tip [13,18,23], leading to toughening [13,18,28]. However, the K_{IC} values reported for them [13,18] are the plane-strain critical-stress intensity factor for cracking mode I (opening or tensile mode) [29,30],

* Corresponding author.
** Correspondence to: X. Wu, State Key Laboratory of Nonlinear Mechanics, Institute of Mechanics, Chinese Academy of Sciences, Beijing 100190, China.
E-mail addresses: ema@jhu.edu (E. Ma), xlwu@imech.ac.cn (X. Wu).

https://doi.org/10.1016/j.scriptamat.2019.07.010
1359-6462/

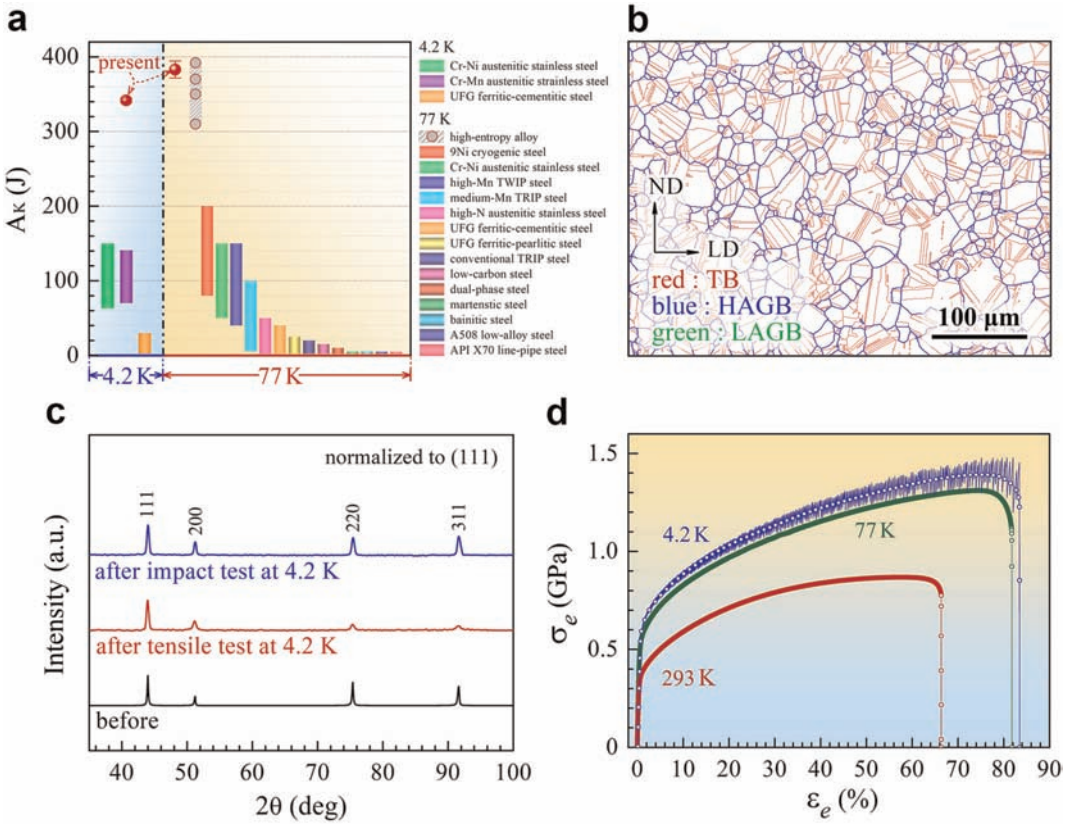

Fig. 1. Microstructure and mechanical properties in CoCrNi MEA. (a) CVN impact fracture toughness (A_K) at 4.2 K and 77 K. All data are with standard full-size CVN samples. (b) EBSD grain boundary image after recrystallization at 1173 K for 2 h. LD and TD denote the longitudinal and transverse directions of sample. (c) XRD spectra showing single phase fcc structure before and after tensile testing and impact loading at 4.2 K. (d) Tensile engineering stress-strain curves at 4.2 K, 77 K, and 293 K, respectively.

neither for impact conditions nor for LHT [13,18]. Very recently, A_K results for the quaternary and quinary HEAs point to superior impact performance (also included in Fig. 1a); but they are for 77 K and above [31–34] and the underlying mechanisms were not analyzed in detail.

The purpose of this paper is two-fold. First, we benchmark the impact toughness using standard Charpy V-notch tests at LHT, for the CrCoNi MEA as a representative of the fcc-HEAs/MEAs. It is a non-trivial task to carry out 4.2 K impact tests that meet standard A_K testing/sample requirements. Our finding fills a hole, as there has been no mechanical test data (including toughness or tensile properties) at LHT so far for HEAs/MEAs. Second, we document the microstructural mechanisms underlying the extraordinary A_k we observe at LHT. In particular, our experimental evidence demonstrates that CrCoNi indeed has the following key ingredients for high A_K at 4 K. First, similar to previous fcc alloys, CrCoNi is a single-phase fcc alloy, which bodes well for both extensive dislocation plasticity and strain hardening, especially at very low temperatures where dynamic recovery is minimal. Second, this MEA is known to have a low SFE [19], favoring DT [18–21]. We project that the impact loading at high strain rates and at LHT would entail elevated driving stress to further promote DT [6,27]. Third, while the SFE is so low to suggest a tendency towards hexagonal-close-packed (hcp) packing [22,35], DT remains the predominant mode of plastic deformation, accompanied by only minor hcp martensite formation [35]. This remains true even when deformed at 4.2 K under impact. A stable austenite is expected to help preserve high A_k. Fourth, we will show that the profuse DT not only serves as the predominant mode to carry extensive plastic deformation and impart high strain hardening, but also in its wake blocks and hardens incipient shear bands (SBs) when strain localization sets in. Such localized strain softening would normally evolve into major SBs as a precursor of cracking under impact loading.

The as-annealed CrCoNi MEA has the chemical composition of 30.7Cr–34.7Co–34.6Ni (wt%). The MTS PTMS4750 pendulum impact tester, equipped with a specially designed liquid helium cryostat, was used for testing A_K at LHT. The Charpy V-notch (CVN) specimen was used with the standard full-size of $10 \times 10 \times 55$ mm^3 and V-notch radius of 0.25 ± 0.025 mm. We also conducted quasi-static tensile tests at a strain rate of 5×10^{-4} s^{-1} at LHT, LNT and RT. The tensile specimens were dog-bone-shaped, with a cross-section of 2×6 mm^2 and a gauge length of 20 mm. Five specimens were used for A_K tests and three for tension and the presented data were the average with standard deviation. Micro-hardness (H_V) tests were conducted using a micro-hardness tester at RT. The microstructural features, together with the propagation path of both the cracks and shear bands (SBs), were investigated using a field-emission scanning electron microscope (SEM), electron backscatter diffraction (EBSD) imaging, and transmission electron microscopy. TEM foil samples, near the tip of either the shear-band or crack and near the fracture surface, were cut using focused ion beam (FIB) micromachining. See Supplementary Information for details of all processing and testing methods.

Fig. 1b is the EBSD grain boundary map of the an-annealed CrCoNi MEA. The average grain size is around 30 μm. Annealing twins are visible inside most grains. The XRD spectra, Fig. 1c, indicate a single fcc phase, before and after impact and tensile testing at LHT. Fig. 1d shows the tensile engineering stress–strain (σ–ε) curves at LHT. The yield strength ($\sigma_{0.2}$), ultimate tensile strength (UTS), and percent elongation to failure all increase simultaneously when compared to those at RT and LNT.

The Charpy V-notch (CVN) impact fracture toughness, A_K, measured as the total absorbed energy upon impact, is 340 ± 2 J at LHT (4.2 K). This data point is shown in Fig. 1a. The previously reported CVN A_K data, all assessed using the standard sample dimensions at LNT and LHT, are also summarized in Fig. 1a. The LHT A_K is on par with the

value at 77 K (including several previously reported other HEAs [31–34]), far better than other alloys [4–8,10], as compared in Fig. 1a. Only a couple of previous alloys can preserve respectable A_K on the order of 100 J around 4.2 K [4,5], considerably lower than their A_K values at RT, the best of which can approach 300 J [6–8].

Fig. 2a shows the crack propagating path during impact, for both the main crack (labeled as C_1) and secondary cracks (e.g. a typical one labeled by C_2). The main crack tip advances forward inside a wide shear band (SB), Fig. 2b. The SB ahead of secondary crack is also seen (Fig. 2c). The micro-void (labeled by v) is found inside the SB, at some distances in front of the crack tip. The elongated deformation bands are visible on both sides of the SB. Apparently, both the SB and micro-voids are precursors on the crack propagation path, which is well known for impact loading [36,37]. This is expected from severely localized plastic strains inside the SB, where damages initiate to instigate crack tip advances [37]. Besides, all five CVN samples were not broken into two pieces at LHT, one sample is shown in Fig. 2d. We quantify strain hardening using Hv measurements. As seen in Fig. 2e, hardening is obvious across a large area of the vertical section of the CVN sample. A band of very high Hv (in crimson) is observed right ahead of the crack tip and along the crack path on the fracture surface. The maximum H_V is as high as 5.4 GPa, far above the initial 2.5 GPa. This indicates extraordinary strain hardening during impact. Interestingly, H_V is higher in the SB center than the outside (Fig. 2f). This indicates that inside the strain concentrated SB there is also a mechanism that hardens the normally strain softening SBs. The corresponding fracture surface exhibits overwhelmingly dimples (Fig. 2g–i), typical of the ductile fracture mode.

Cracking follows the path of the advancing SB [36,37], where plastic strains are localized to cause the emergence, growth and coalescence of micro-voids [36,37]. The high A_K implies that the vast majority of

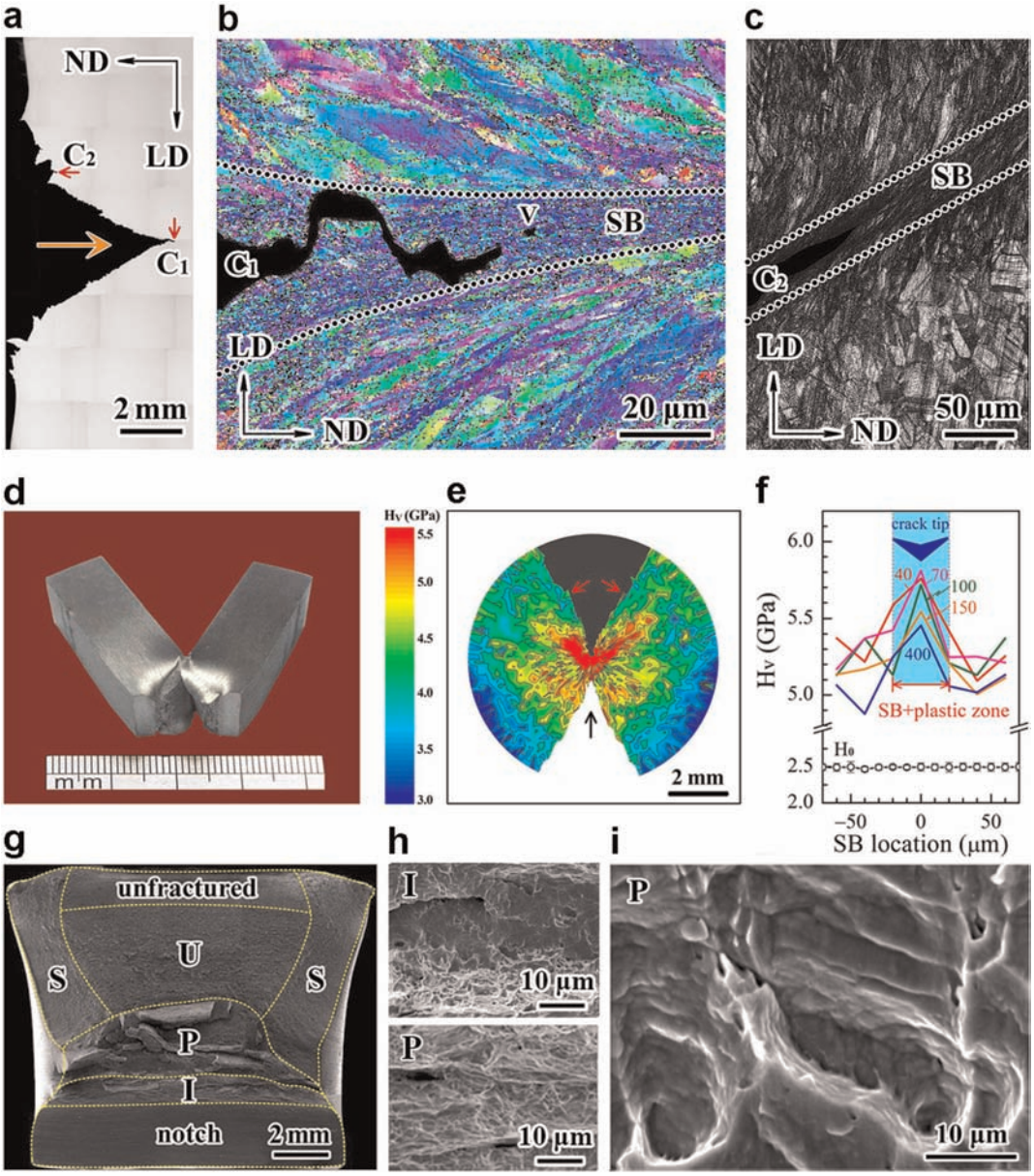

Fig. 2. Cracking behavior and fractographic morphology after impact loading of CVN sample at 4 K. (a) SEM image of crack propagation path. C_1: main crack. C_2: secondary crack. Big orange arrow: crack propagating direction. Small red arrow: crack tip. (b, c) Close-up views at the tip of C_1 and C_2. SB: shear band outlined by dotted line in (b). v: micro-void. LD and TD: longitudinal and transverse directions. (d) Un-broken CVN sample after Charpy loading. (e) Hv distribution labeled by scale bar (left) around the V-notch and along fracture surface. Red arrows: fracture surface. Black arrow: pendulum hitting direction. (f) H_V values across the SB at varying distances (number, μm) away from the tip of main crack. Blue area: SB and surrounding plastic zone. H_0: initial H_V before impact loading. Blue arrow: main crack tip. (g) Fracture surface. I: initiation of crack, P: stable crack propagation, U: unstable propagation, S: shear-lip. (h) Close-up views of area I (upper panel) and P (lower panel), showing a consistent dimpled ductile fracture associated with extended tearing ridges, dimples, and delamination. (i) Dimples in P. (For interpretation of the references to color in this figure legend, the reader is referred to the web version of this article.)

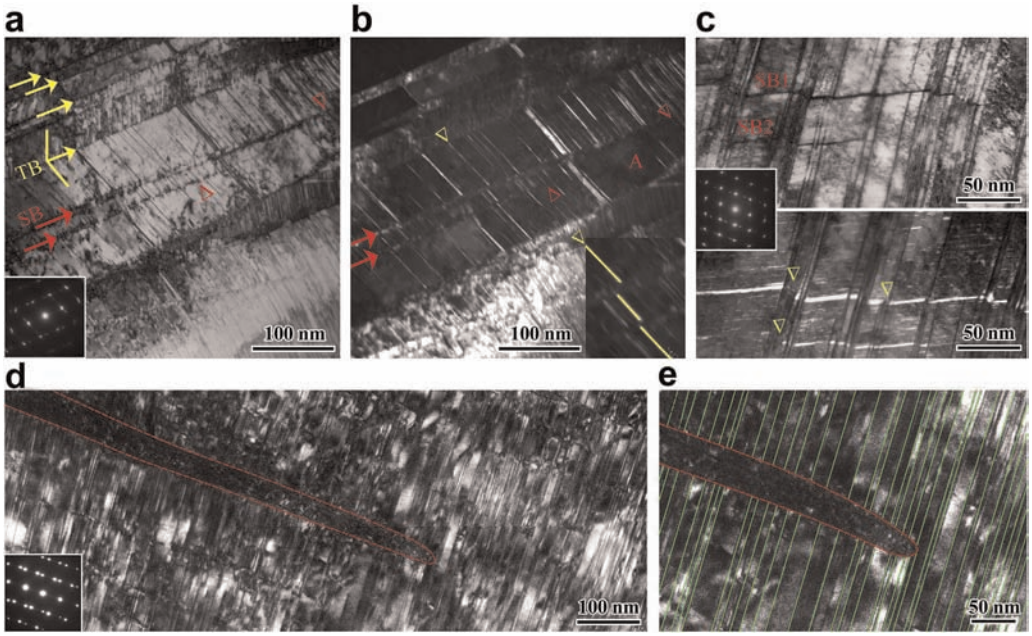

Fig. 3. TEM micrographs showing the blockage of incipient shear bands by twin boundaries. (a) Bright-field image showing primary twins and thin shear bands. TB: twin boundaries labeled by yellow arrows. SB: shear band labeled by red arrows. Red tri-angle: the endpoint of SB. (b) Dark-field image of secondary twins in one primary twin. Red arrows: SBs. Inset: close-up showing the offset of twin plates by two SBs, at the location marked by a yellow tri-angle. (c) Bright-(upper) and dark-field (lower) images showing two SBs and primary twins and disrupted propagation of SBs. (d) Blockage of SB, outlined by red dashed line, by primary twins of very small twin spacing (average spacing of 6 nm). (e) Close-up view showing the cut-off and relative shift of nanotwins of the SB. Insects in (a), (c), and (d) are selected area electron diffraction patterns showing the twin orientation relationship. (For interpretation of the references to color in this figure legend, the reader is referred to the web version of this article.)

incipient SBs have been prevented from becoming major SBs that mediate crack propagation. We therefore examine some small SBs to see how they are blocked by DT-mediated plasticity that delocalizes the deformation strain. Fig. 3a is a TEM image. Several parallel primary twins pass through a grain interior, which is located close to the front end of a propagating SB. Several thin SBs (red arrows) traverse twin plates. Inside the primary twin, secondary twins of high density are visible, with an average twin spacing of ~10 nm. As clearly seen in Fig. 3b, SBs propagate through secondary twins. As a result, these twins are cut apart into two pieces [38]. The inset is a close-up view showing the offsetting shift of a twin plate (marked using yellow triangle) along the propagating direction of SBs, after the SBs cut the plate apart. Both SBs terminate their propagation inside the twin plate. Hence, these secondary twins, triggered in response to shear banding (more obvious in front of SB where there is intensified strain rates and stress concentration [36,37] than at the trailing end of an advancing SB), block SB propagation. Also note area A with nearly no secondary twins, in contrast to the area with secondary twins of high density on the other side of the SB. This is probably due to de-twinning [25], which happens due to stress relaxation after the SB growth, leaving short twin segments at grain boundaries (Fig. 3b). Meanwhile, primary twins that form continuously and dynamically along with deformation also effectively obstruct the propagating SBs, see Fig. 3c (upper panel). The SB propagates in a discontinuous, i.e., disrupted, manner (lower panel). Hence, both the primary and secondary twins weave a twin boundary net to restrain the SBs (Fig. 3a). As a result, deformation twins not only store a high density of twin boundaries to provide strong strain hardening, they also prevent most of the small SBs from developing into major ones that could mediate crack advances. Fig. 3d shows another example of primary twins to block a propagating SB. Fig. 3e is the close-up showing clearly the cut-off of nanotwins by this SB. Note the twin spacing is only 6 nm, suggesting strong strain hardening capability [27]. In other words, even when strain localization takes place, there will be secondary DT ahead of a SB tip, reducing the tendency for SB widening. Moreover, the secondary twins and grain refinement also happen inside the SB to cause strain hardening that suppresses the micro-voiding inside the band. This self-toughening alleviates the softening in SBs that would otherwise lead to void formation and later crack propagation.

Speaking of grain refinement, Fig. 4a shows a SB traversing a twin plate, with close-up views of the two boxed areas. In Fig. 4b (box 1), the severely deformed layer (SDL) is seen between the twin and matrix; the left one against the propagating SB is wider than that on the right side. The 2D lattice becomes undistinguishable in this image, mainly due to the generation of a high density of dislocations. This heavy local deformation is typical, when SB runs into the twin boundary at high speeds, see also Fig. 4c for area 2.

Such microstructural refinement can be seen across the plastic zone around the SB tip. Fig. 4d shows the tips of several SBs, which terminate in a grain interior. Several parallelogram-shaped nanodomains are seen exactly near the SB tip (Fig. 4e), as marked by arrows indicating their side edges/faces. As seen in Fig. 4f, the sides are either a stacking fault (SFs also contribute to strain hardening [39]) or a micro-twin plate of only 2–3 atomic layers thick. This indicates that the partial dislocations are activated at the SB tip, where the large stresses trigger the emission of partials, forming either SFs or twins [40]. Fig. 4g shows the formation of nanoscale domains near SBs.

It is in fact known that for some fcc metals and alloys, the ductility increases rather than decreases, upon lowering the tensile test temperature. This is due to suppressed dynamic recovery at lower temperatures, rendering effective dislocation storage and hence efficient strain hardening to prolong uniform tensile elongation [41]. In recent papers, the enhancement of tensile ductility of the low-SFE CrCoNi MEA has already been discussed, in terms of more pronounced deformation twinning and dislocation accumulation at cryogenic temperatures [42–44]. Here deformation twinning is promoted due to not only higher driving stresses, but also further reduced magnitude of SFE, in cold tensile samples at, e.g., liquid nitrogen temperature. Similar effects of SFE on the propensity for deformation twinning and defect storage are also known for steels, where SFE can be tuned by changing the Mn content [45].

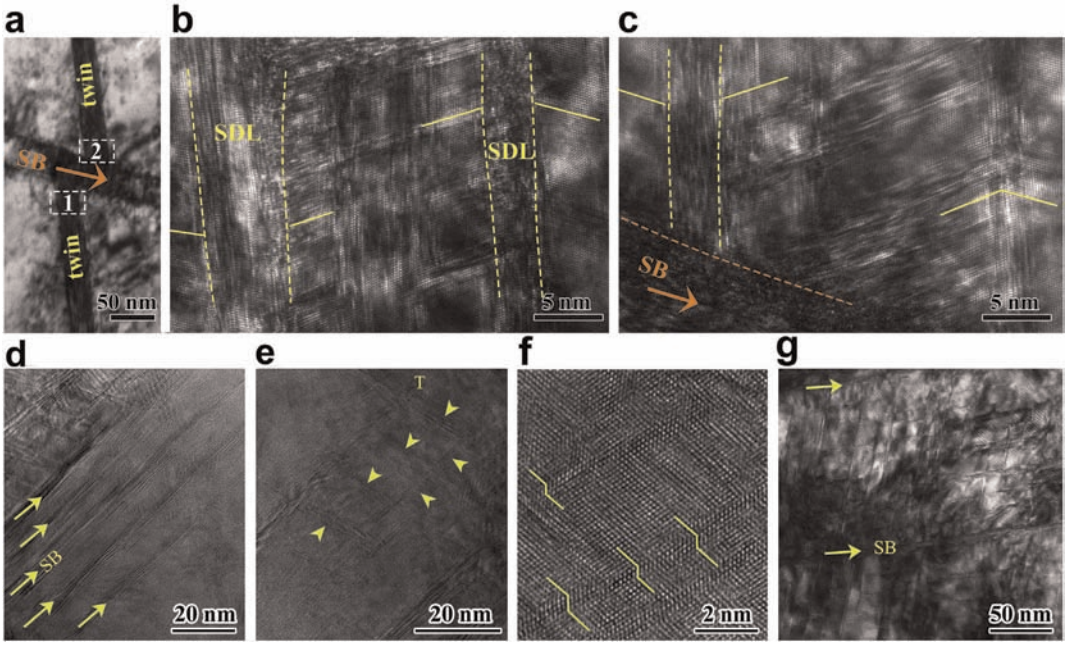

Fig. 4. TEM micrographs showing interaction between shear bands and twin boundaries and nano-domains induced by shear-banding. (a) Shear band (SB) traversing a twin plate, causing a relative shift between two twin segments along the SB. (b, c) Close-up views of two squared areas (1 and 2, respectively) in (a). A severe deformation layer (SDL) outlined by two dashed lines evolved from the original twin boundary. The two sides of the SDL keep their twin orientation relationship, as marked using two yellow lines. (d) Several shear bands (SB) (indicated by arrows) inside a grain. (e) Close-up view at the SB tip in (d). Parallelogram-shaped nanodomains are clearly seen. Triangles indicate their sides. (f) Close-up view of nanodomains in (d). Parallelogram sides of stacking faults and micro-twins are indicated by yellow lines. (g) Low magnitude of nanodomains of high density near a SB. (For interpretation of the references to color in this figure legend, the reader is referred to the web version of this article.)

The strain rate in LHT A_K testing is ~10^3 s^{-1} [30], several orders higher than K_{IC} tests (LNT) [13,18,28]. As a result, the alloy strength is much higher, which inversely scales with the size of the plastic zone and would reduce toughness. Comparing the A_K of our MEA at LHT with that at LNT (see Fig. 1a), there is a minor but visible reduction in toughness. This is likely a result of the decrease of the plastic zone size due to elevated yield strength: the volume experiencing strain hardening decreases at 4 K relative to that at 77 K. However, this adverse effect on A_k is countered-balanced by the increasing DT-induced hardening (with decreased twin spacing), so the A_k does not drop significantly at 4 K. The fcc-to-hcp transformation was not observed in all samples tested at both temperatures.

In summary, the DT activities and defect interactions are intensified by the high driving stresses at LHT and impact rate. A large number of primary and secondary twins are incessantly embedded into the microstructure upon dynamic loading. This carries large plastic deformation throughout a wide plastic zone ahead of the crack tip, causing work hardening and relieving locally high stresses, and stops strain localization dead in its tracks to delay the formation of major shear bands for crack propagation (it is well known that brittle cleavage can occur when crack propagation is along the Σ3{111} coherent twin boundaries [46]). All above mentioned behaviors dissipate a considerable amount of energy to prevent cavitation and cracking. The CrCoNi MEA therefore preserves a record-high toughness, despite of the high strain rate and liquid-helium temperature, Fig. 1a. The results confirm our idea that the cryogenic temperature and high-rate loading best exploit the high DT propensity in this low-SFE alloy. This is compounded by the advantage that in this MEA DT remains overwhelming without conceding to martensitic transformation, which would degrade toughness. This case shows an example of the advantages of the emerging multi-principal element alloys that are currently attracting much attention. A useful hallmark of the fcc single-phase HEAs/MEAs is then these new concentrated solution alloys rival the best cryogenic alloys, such as austenitic stainless steels, in terms of all-around tensile and toughness properties at all temperatures. These new alloys thus expand the repertoire for materials selection, especially at temperatures in the LNT-LHT regime.

Acknowledgements

X.W. and F.Y. were funded by the National Key Research and Development Program of China 2017YFA0204402, the Natural Science Foundation of China (Grant Nos. 11572328, 11672313, and 11790293), the Strategic Priority Research Program of the Chinese Academy of Sciences (Grant No. XDB22040503). E.M. was supported at JHU by US NSF-DMR1804320.

Appendix A. Supplementary data

Supplementary data to this article can be found online at https://doi.org/10.1016/j.scriptamat.2019.07.010.

References

[1] M.F. Ashby, Acta Metall. 37 (1989) 1273–1293.
[2] M.E. Launey, R.O. Ritchie, Adv. Mater. 21 (2009) 2103–2110.
[3] R.O. Ritchie, Nat. Mater. 10 (2011) 817–822.
[4] T.S. Byun, T.G. Lach, Mechanical properties of 304L and 316L austenitic stainless steels after thermal aging for 1500 hours. U.S. Department of Energy, 2016, DE-AC05-76RL01830.
[5] P. Duthil, Material Properties at Low Temperature. Institut de Physique Nucléaire d'Orsay, 2015, arXiv:1501.07100.
[6] Y. Tomota, J. Nakano, Y. Xia, K. Inoue, Acta Mater. 46 (1998) 3099–3108.
[7] C.K. Syn, J.W. Morris, S. Jin, Metall. Trans. A. 7 (1976) 1827–1832.
[8] J. Han, A.K. da Silva, D. Ponge, D. Raabe, S.M. Lee, Y.K. Lee, S.I. Lee, B. Hwang, Acta Mater. 122 (2017) 199–206.
[9] A.H. Cottrell, Trans. Metall. Soc. AIME 212 (1958) 192–203.
[10] Y. Kimura, T. Inoue, F.X. Yin, K. Tsuzaki, Science 320 (2008) 1057–1060.
[11] M.H. Tsai, J.W. Yeh, Mater. Res. Lett. 2 (2014) 107–123.
[12] Y.F. Ye, Q. Wang, J. Lu, C.T. Liu, Y. Yang, Mater. Today 19 (2016) 349–362.
[13] B. Gludovatz, A. Hohenwarter, D. Catoor, E.H. Chang, E.P. George, R.O. Ritchie, Science 345 (2014) 1153–1158.
[14] Z.M. Li, K.G. Pradeep, Y. Deng, D. Raabe, C.C. Tasan, Nature 534 (2016) 227–230.
[15] T. Yang, Y.L. Zhao, Y. Tong, Z.B. Jiao, J. Wei, J.X. Cai, X.D. Han, D. Chen, A. Hu, J.J. Kai, K. Lu, Y. Liu, C.T. Liu, Science 362 (2018) 933–937.
[16] Z. Lei, X. Liu, Y. Wu, H. Wang, S. Jiang, S. Wang, X. Hui, Y. Wu, B. Gault, P. Kontis, D. Raabe, L. Gu, Q. Zhang, H. Chen, H. Wang, J. Liu, K. An, Q. Zeng, T.G. Nieh, Z. Lu, Nature 563 (2018) 546.
[17] S.S. Sohn, A. Kwiatkowski da Silva, Y. Ikeda, F. Körmann, W. Lu, W. Choi, B. Gault, D. Ponge, J. Neugebauer, D. Raabe, Adv. Mater. (2019) 1807142.

[18] B. Gludovatz, A. Hohenwarter, K.V.S. Thurston, H.B. Bei, Z.G. Wu, E.P. George, R.O. Ritchie, Nat. Commun. 7 (2016) 10602.
[19] Z.J. Zhang, H.W. Sheng, Z.J. Wang, B. Gludovatz, Z. Zhang, E.P. George, Q. Yu, S.X. Mao, R.O. Ritchie, Nat. Commun. 8 (2017) 14390.
[20] M.X. Yang, D.S. Yan, F.P. Yuan, P. Jiang, E. Ma, X.L. Wu, Proc. Natl. Acad. Sci. U. S. A. 115 (2018) 7224–7229.
[21] C.E. Slone, J. Miao, E.P. George, M.J. Mills, Acta Mater. 165 (2019) 496–507.
[22] S. Huang, H. Huang, W. Li, D. Kim, S. Lu, X. Li, E. Holmström, S.K. Kwon, L. Vitos, Nat. Commun. 9 (2018) 2381.
[23] Y. Ma, F.P. Yuan, M.X. Yang, P. Jiang, E. Ma, X.L. Wu, Acta Mater. 148 (2018) 407–418.
[24] Z. Fu, L. Jiang, J.L. Wardini, B.E MacDonald, H. Wen, W. Xiong, E.J. Lavernia, Sci. Adv. 4 (2018) e8712.
[25] Y.T. Zhu, X.Z. Liao, X.L. Wu, Prog. Mater. Sci. 57 (2012) 1–62.
[26] L. Lu, X. Chen, X. Huang, K. Lu, Science 323 (2009) 607–610.
[27] K. Lu, L. Lu, S. Suresh, Science 324 (2009) 349–352.
[28] S.W. Kim, X.Y. Li, H.J. Gao, S. Kumar, Acta Mater. 60 (2012) 2959–2972.
[29] R.O. Ritchie, B. Francis, W.L. Server, Metall. Trans. A. 7 (1976) 831–838.
[30] T. Lin, A.G. Evans, R.O. Ritchie, Acta Metall. 34 (1986) 2205–2216.
[31] D. Li, Y. Zhang, Intermetallics 70 (2016) 24–28.
[32] S.Q. Xia, M.C. Gao, Y. Zhang, Mater. Chem. Phys. 210 (2018) 213–221.
[33] J.H. Kim, K.R. Lim, J.W. Won, Y.S. Na, H.S. Kim, Mater. Sci. Eng. A712 (2018) 108–113.
[34] M.A. Laktionova, E.D. Tabchnikova, Z. Tang, P.K. Liaw, Low Temp. Phys. 39 (2013) 630–632.
[35] C. Niu, C.R. LaRosa, J. Miao, M.J. Mills, M. Ghazisaeidi, Nat. Commun. 9 (2018) 1363.
[36] M. Zhou, A.J. Rosakis, G. Ravichandran, J. Mech, Phys. Solids 44 (1996) 981–1006.
[37] Z. Zhang, R.J. Clifton, J. Mech, Phys. Solids 51 (2003) 1903–1922.
[38] C.S. Hong, N.R. Tao, X. Huang, K. Lu, Acta Mater. 58 (2010) 3103–3116.
[39] W.W. Jian, G.M. Cheng, W.Z. Xu, H. Yuan, M.H. Tsai, Q.D. Wang, C.C. Koch, Y.T. Zhu, S.N. Mathaudhu, Mater. Res. Lett. 1 (2013) 61–66.
[40] X.L. Wu, Y.T. Zhu, Appl. Phys. Lett. 89 (2006), 031922.
[41] R. Abbaschian, L. Abbaschian, R.E. Reed-Hill, Physical Metallurgy Principles, 4th ed. Cengage Learning Inc., Stamford, CT, 2008 521–560.
[42] F. Otto, A. Dlouhý, C. Somsen, H. Bei, G. Eggeler, E.P. George, Acta Mater. 61 (2013) 5743–5755.
[43] G. Laplanche, A. Kostka, O.M. Horst, G. Eggeler, E.P. George, Acta Mater. 118 (2016) 152–163.
[44] G. Laplanche, A. Kostka, C. Reinhart, J. Hunfeld, G. Eggeler, E.P. George, Acta Mater. 128 (2017) 292–303.
[45] B.B. He, B. Hu, H.W. Yen, G.J. Cheng, Z.K. Wang, H.W. Luo, M.X. Huang, Science 357 (2017) 1029–1032.
[46] D.C. Jang, X.Y. Li, H.J. Gao, J.R. Greer, Nat. Nanotechnol. 7 (2012) 594–601.